AlScN-on-SiC Diaphragm Multimode Micromechanical Resonators for High-Temperature Sensing Applications

Wen Sui[1*], Haoran Wang[1], Jaesung Lee[1], Afzaal Qamar[2], Mina Rais-Zadeh[2,3], and Philip X.-L. Feng[1*]

[1]Department of Electrical & Computer Engineering, Herbert Wertheim College of Engineering,
University of Florida, Gainesville, FL 32611, USA

[2]Department of Electrical Engineering & Computer Science, College of Engineering,
University of Michigan, Ann Arbor, MI 48109, USA

[3]NASA Jet Propulsion Laboratory, California Institute of Technology, Pasadena, CA 91109, USA

[*]Email: wen.sui@ufl.edu, philip.feng@ufl.edu

Abstract

We demonstrate circular diaphragm multimode micromechanical resonators made of heterostructure thin film of aluminum scandium nitride (AlScN) sputtered on cubic silicon carbide (3C-SiC). We systematically characterize the multimode resonators from room temperature up to 600ºC high-temperature environment. We observe clear consistency in resonances measured in heating up and cooling down processes, validating that the AlScN/SiC diaphragm resonators can operate robustly in high-temperature environment up to 600˚C without observable degradation. Raman spectroscopy results indicate that the turning points of the peak positions of the longitudinal optical (LO) phonon modes of both 3C-SiC and AlScN occur in almost the same temperature region where the turning point of temperature coefficient of resonance frequency (TCf) is observed. We calibrate the device temperature by measuring Raman peak of the silicon (Si) substrate of the chip, yielding a crystal lattice temperature of 410ºC at the heater setting temperature being 600ºC. The heating efficiency can be improved by clamping the chip using a clip or jig with lower thermal conductivity.

Keywords

Aluminum Scandium Nitride (AlScN), Silicon Carbide (SiC), Diaphragm, Resonator, High Temperature, Harsh Environment, Micro/nanoelectromechanical Systems (MEMS, NEMS)

I. Introduction

Microelectromechanical systems (MEMS) offer attractive characteristics such as high precision, high responsivity, and low power consumption, which are crucial for many technologically important industries such as biomedical, automotive, military, and aerospace. [1,2]. While Si MEMS have prevailed in mainstream sensors, the electronically transduced Si MEMS are unsuitable for high-temperature applications due to failing of Si electronics at ~350ºC and degradation of Si mechanical properties at above 500ºC [3]. In various critical applications, one important and urgent mission is to develop MEMS sensors capable of operating in harsh or extreme environments with very high temperature, corrosion, and radiation [4,5]. Researchers have investigated materials which are intrinsically more tolerant to these extreme cases. Thanks to the superior physical and chemical properties, wide-bandgap materials such as III-nitride, silicon carbide (SiC), and diamond-like carbon (DLC) have emerged as valid alternatives to Si for MEMS operating in harsh environments [6,7]. Recent development in combining

AlN and SiC offers exciting opportunities for building MEMS operating in high-temperature environments, so as to possibly integrate the high-temperature sustainable and durable piezoelectricity in AlN and the outstanding mechanical and thermal properties of SiC, as well as advanced micromachining techniques, along with the commercial availability of both 3C-SiC wafers and AlN custom processes [8,9]. In this work, we demonstrate AlScN/SiC heterostructure circular diaphragm multimode resonators operating in high-temperature environment up to 600˚C. We investigate both device-level and atomic level vibrations in AlScN/3C-SiC diaphragm resonators at varying temperature by using ultrasensitive optical interferometry techniques and Raman spectroscopy.

II. Results and Discussions

A. XRD Analysis of the AlScN/SiC Heterostructure on Si

Single-crystal n-type 3C-SiC (100) thin film with the thickness of 900 nm is grown on Si (100) substrate by low

pressure chemical vapor deposition (LPCVD) process. 1μm-thick AlScN with 20% Sc is then sputtered on top of the 3C-SiC epilayer on Si substrate. After the growth process, X-ray diffraction (XRD) analysis of the grown film is carried out to confirm the crystal structure and quality. Fig. 1 shows the XRD results of the AlScN/3C-SiC heterostructure on Si obtained in conventional θ-2θ scan mode. We observe the peaks corresponding to the (100) plane for the SiC layer, which indicates that single-crystal 3C-SiC (100) is grown on Si (100). Three peaks are observed for AlScN, which confirms the polycrystalline nature with the preferred orientation along the c-axis, *i.e.*, AlScN (002) peak.
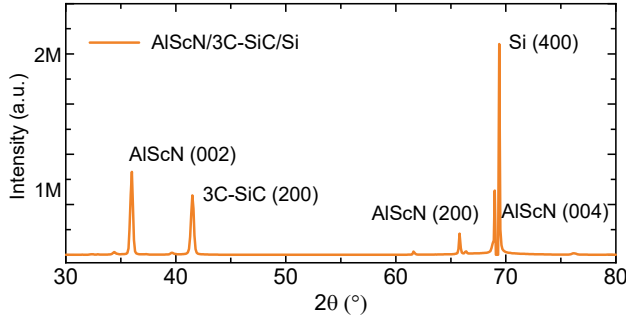

Fig. 1. XRD analysis of the AlScN/3C-SiC heterostructure on Si.

B. *TEM Imaging of the AlScN/SiC Interface*

Fig. 2 shows the transmission electron microscopy (TEM) image of the AlScN/SiC interface, which clearly displays the columnar growth of AlScN film. Grain boundaries are not observed in the 3C-SiC thin film, while the main defects are stacking faults well known in 3C-SiC grown on Si. The selected area electron diffraction (SAED) pattern reinforces the XRD results and confirms that the 3C-SiC layer is single-crystalline, and the AlScN thin film is polycrystalline.
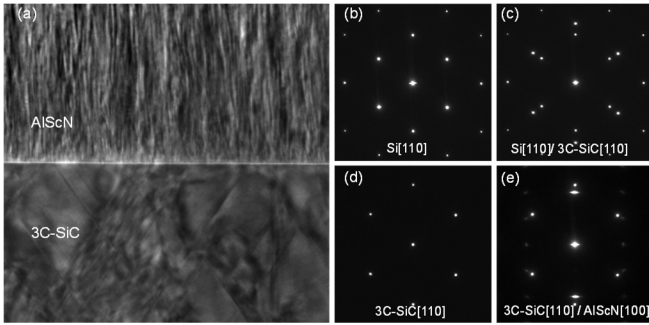

Fig. 2. (a) TEM cross-sectional image of the AlScN/3C-SiC interface. SAED patterns of (b) Si, (c) 3C-SiC, (d) 3C-SiC/Si, and (e) 3C-SiC/AlScN in the [110] orientation.

C. *Device Fabrication*

The fabrication process starts from the back side to form the suspended AlScN/SiC diaphragms. First, 500 nm Al_2O_3 thin

film is sputtered on the back side and then patterned by the photolithography and wet etching, to act as the hard mask for deep etching of Si. Circular diaphragms with diameters varying from 250 μm, 500 μm, 750 μm, to 1 mm are designed and patterned on the Al_2O_3 mask (Fig. 3b). After that, the Si substrate with a thickness of around 650 μm is removed by deep reactive ion etching (DRIE) to form suspended AlScN/SiC diaphragms (Fig. 3c). The process is carefully controlled to maintain the anisotropic etching with vertical sidewalls, and it stops when the embedded SiC layer is exposed. Fig. 3d and 3f show an optical image of the released diaphragm in the front-side view and an SEM image of the etched cavity in the back-side view, respectively. The diaphragm has a diameter of 500 μm, consistent with the design, and well defined by the DRIE process. Larger diaphragms can have buckling due to stress.
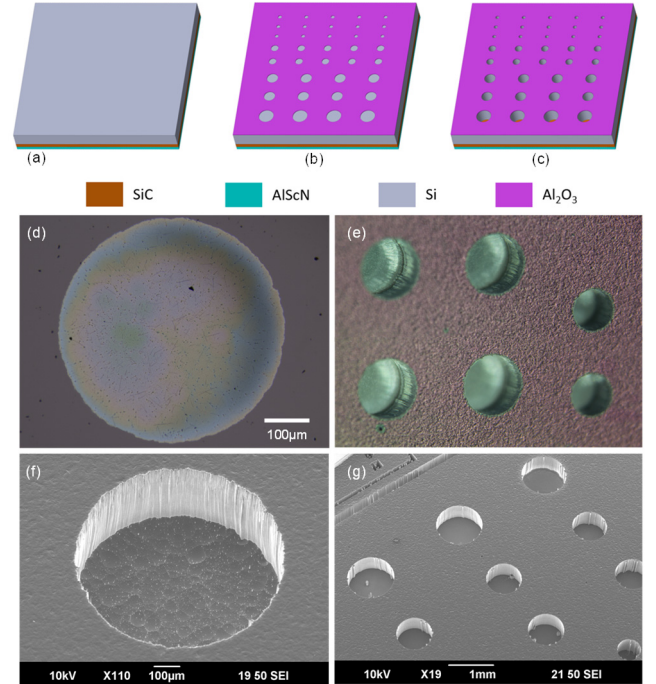

Fig. 3. (a)-(c) Fabrication process flow. Optical image of (d) a circular diaphragm with d =500 μm in the front-side view, and (e) an array of the fabricated diaphragms. SEM image of (f) the etched cavity with d =500 μm in the back-side view, and (g) an array of the fabricated diaphragms.

D. *Experimental Techniques*

The multimode resonances of the AlScN/SiC resonator are measured by using a laser interferometry system, as shown in Fig. 4. We photothermally excite the resonances with an intensity-modulated 405 nm blue laser, and employ a 633 nm He-Ne laser to detect the vibration. Dynamic interference occurs between the light reflected by the vibrating diaphragm and that by the substrate surface below the suspended structure. A photodetector converts the time-varying optical

interferometric signals into electronic signals and the frequency response is read out by a network analyzer [10]. The temperature is regulated from room temperature up to 600ºC by using a customized heating and sensing system. Raman measurements are performed using a customized micro-Raman system integrated into the laser interferometry system to trace the evolution of stress and the quality of the crystal at varying temperatures [11].
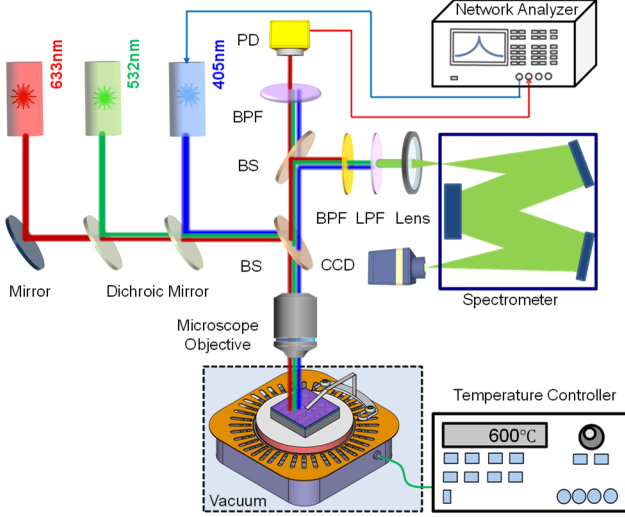

Fig. 4. Schematic illustration of the combined Raman spectroscopy and interferometry system configured with a precisely temperature-controlled device stage. BPF, PD, and BS represent a band-pass filter, a photodetector, and a beam splitter, respectively.

E. Temperature-Dependent Multimode Resonances

We first characterize the multimode resonances of a AlScN/SiC diaphragm with diameter of 250 μm. As shown in Fig. 5a, totally four resonance modes are observed in the range of 700 to 1000 kHz at room temperature, specifically, $f_1 = 788$ kHz, $f_2 = 827$ kHz, $f_3 = 850$ kHz, $f_4 = 899$ kHz. Both mode 1 and mode 4 show a clear single resonance peak, while mode 2 and mode 3 show more complicated peaks, which may be ascribed to the asymmetry arising from the uneven roughness of the back side. When the temperature increases to 600 ºC, the resonance frequency of the 1st mode slightly decreases to 784 kHz, while the frequency increases for all the higher order modes. We then characterize the temperature coefficient of resonance frequency (TCf) of the first two resonance modes from 25ºC up to 600ºC. Fig. 6a,b depict the resonance frequencies of the first two modes measured as function of temperature for both the heating and cooling periods. Overall, we observe clear consistency in resonances for both modes measured during heating and cooling processes, validating the AlScN/SiC diaphragm resonators can operate reliably at high temperature up to 600ºC without observable degradation. Interestingly, modes 1 and 2 exhibit different temperature-dependent resonance behavior. Specifically, the resonance frequency of the 1st

mode slightly increases in the temperature range between 25ºC to 100ºC, and then monotonically decreases as the temperature further increases up to 600 ºC (Fig. 6a). However, a monotonic increase of frequency is observed from the 2nd mode; and temperature dependence is more significant when the temperature is above 400ºC (Fig. 6b).
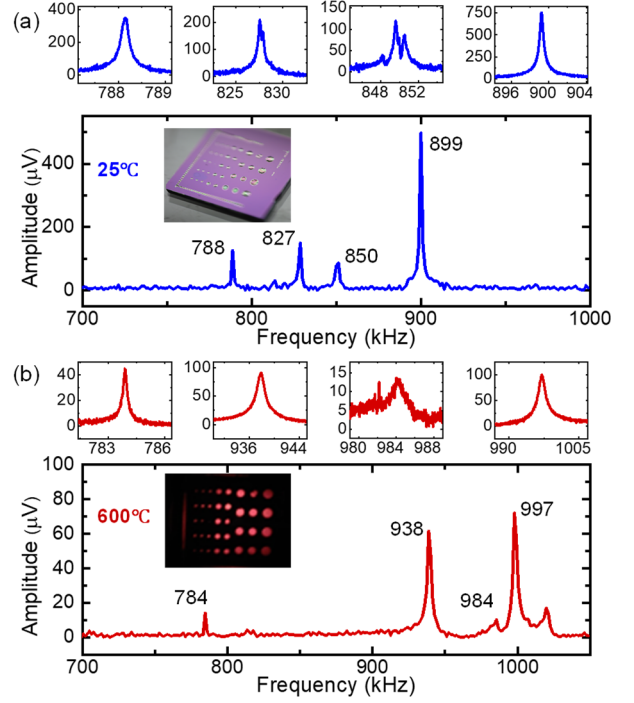

Fig. 5. Measured multimode resonance spectra for a AlScN/SiC device with diameter of 250μm, at (a) 25 ºC and (b) 600 ºC.
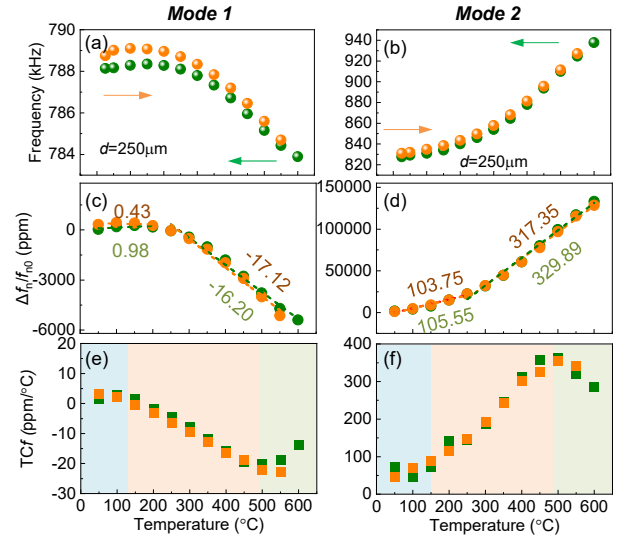

Fig. 6. Measured temperature-dependent resonance frequencies for the (a) 1st mode and (b) 2nd mode. (c)-(d) Fractional frequency shift $(\Delta f_n / f_{n0})$ with varying temperature for the first two modes, where f_{n0} is the frequency measured at room temperature. The averaged TCf is obtained by linear fitting of the $\Delta f_n / f_{n0}$ vs temperature plot. (e)-(f) TCf versus temperature, where the TCf at different temperatures is calculated by $TCf(T) = (1/f(T)) \times (\Delta f / \Delta T)$.

We plot the frequency shift at different temperatures with respect to its resonance frequency at room temperature for mode 1 and mode 2 in Fig. 6c and 6d, respectively. As for mode 1, we observe almost constant fractional shift of frequency ($\Delta f/f$) values within the temperature range from ~25 to 200°C, with an average TCf of less than 1 ppm/°C. However, when the temperature is above 200°C, we observe a linear downshift relation between $\Delta f/f$ and T, with an average TCf of -17 ppm/°C. Note that two segments of linear upshift of fractional frequency are observed from the 2nd mode within the same measured temperature range. Below 200°C, the TCf is evaluated to be about 104 ppm/°C, which is about 1/3 of that measured in higher temperature region, with the average TCf of about 320ppm/°C in the temperature range between 200°C and 600°C. To better understand the temperature-dependent resonance measured from the two modes, we then calculate the TCf at each temperature by using the resonance frequencies measured at two adjacent temperatures (see Fig. 6e-f). Interestingly, we observe a turning point in the TCf plot for the two modes at ~100°C and ~500°C. Such complicated variation of TCf is determined by the competing effects of built-in stress, Young's modulus, as well as thermal expansion properties.

F. Temperature-Dependent Raman Characterization

To better understand the microscopic vibrations in the crystal lattice at varying temperature, we use Raman spectroscopy to study the optical phonon shifts. Fig. 7a,b show the typical Raman spectra of AlScN/SiC sample measured at room temperature and at 600°C from the suspended region where Si is etched away from the back side.

We observe two clear peaks at 646 and 876 cm^{-1} in the room-temperature Raman spectra measured from Si-etched window region, which corresponds to the E$_2$ (high) and A$_1$ (LO) phonon modes of AlScN [12,13], with the full width at half maximum (FWHM) of 29 and 20 cm^{-1}, respectively. Compared to the Raman spectrum of AlN, the incorporation of Sc atoms results in a redshift and broadening of the Raman peaks, which represents a softening of the lattice and an increased scattering rate of the optical phonons. Such behavior originates from the decrease of covalent bond strength and the increase of average atomic mass by replacing Al atoms with Sc atoms. We also observe the typical optical phonon mode of the transverse optical (TO) and the longitudinal optical (LO) phonon modes of 3C-SiC, peaking at around 796 and 973 cm^{-1} in the spectral bands [14,15].

As the temperature increases up to 600°C, a softening (redshift) of the phonon frequencies is observed for both the E$_2$ (high) and A$_1$ (LO) phonon modes of AlScN. However, the two phonon modes of SiC presents opposite response to substrate heating. We observe a redshift for TO mode and a blueshift for LO mode. Note that the turning point of the peak

position of the LO mode of 3C-SiC (Fig. 7d) occurs at almost the same temperature region where the turning point of TCf is observed, which indicates that the microscopic vibrations in the crystal lattice at varying temperature dominates the macroscopic vibration of the diaphragm. As for AlScN, the A$_1$ mode is typically used to characterize the residual stress in AlScN. Similar to what has been observed in the LO mode of 3C-SiC, we observe wo turning points appearing near the two ends of the temperature range in Fig. 7f. Thus, it is reasonable to claim that the shift of resonance frequency with temperature can be attributed to the change of residual stress within the AlScN/SiC stack.
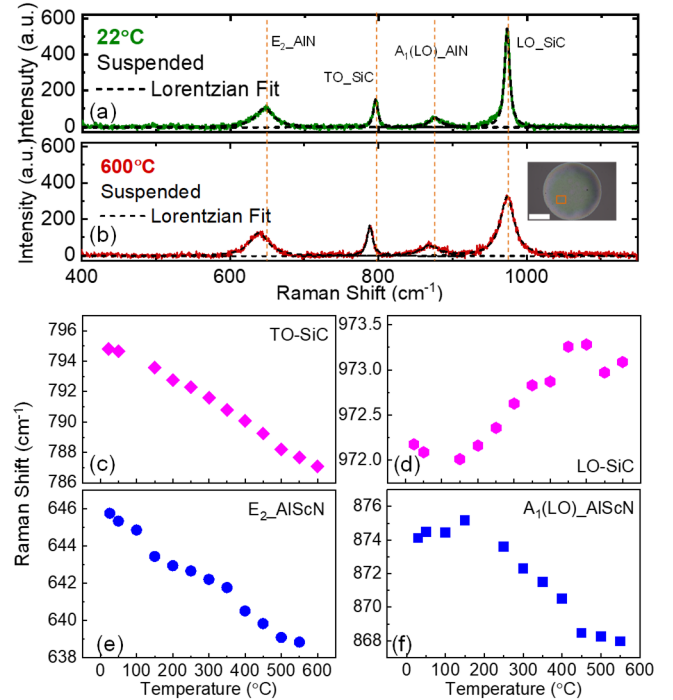

Fig. 7. Raman spectra of suspended AlScN/SiC diaphragm measured at (a) 25°C and (b) 600°C. Insets show the optical microscopy images, with the box labeling the location where data are taken. Lorentzian fitting is shown for data in (a) and (b). Scale bar: 100 μm. Temperature dependence of the peak position of (c) TO-$_{SiC}$ mode, (d) LO-$_{SiC}$ mode, (e) E$_{2-AlScN}$ mode and (f) A$_{1(LO)-AlScN}$ mode with temperature increasing from 25°C to 600°C.

G. Temperature Calibration Based on Si Raman

As shown in Fig. 8, the center position of Si Raman peaks redshifts linearly as the temperature increases from room temperature up to 600°C. We observe a high degree of consistency of the peak position between the heating and cooling cycles when temperature is above 300°C. However, the blueshift of Si peak becomes slower under 300°C due to the slow heat dissipation process. To check the efficiency of our heating stage, we investigate different clamps, including Ruthenium (Ru) probes, SUS340 clamping jig, and ceramic, to mount the sample and calibrate the temperature based on the center position of Si Raman peaks. As shown in Fig. 9,

the temperature reading from Si Raman peak is about 345°C at the heater setting temperature of 600°C when the chip is mounted by Ru probes. Such a large temperature difference (low heating efficiency) originates from the large thermal conductivity of Ru ($\kappa\approx$151W/mK). To verify this point, we mount the chip with SUS340 clamping jig ($\kappa\approx$15–20W/mK) and we then insert a small piece of ceramic with the thermal conductivity of approximately only 3.8W/mK between the SUS340 clamping jig and the chip. The temperature reading from Si Raman peak is 385°C and 410°C, respectively, at the heater setting temperature of 600°C. It is reasonable to claim that the heating efficiency is expected to be further improved by using a clamping jig with lower thermal conductivity.
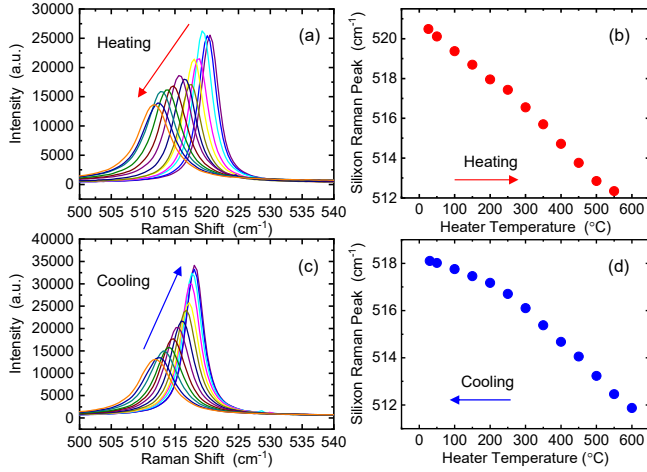

Fig. 8. The center peak position of Si Raman mode as a function of temperature for (a), (b) heating and (c), (d) cooling processes, with the chip mounted on heater and clamped by a SUS340 jig.
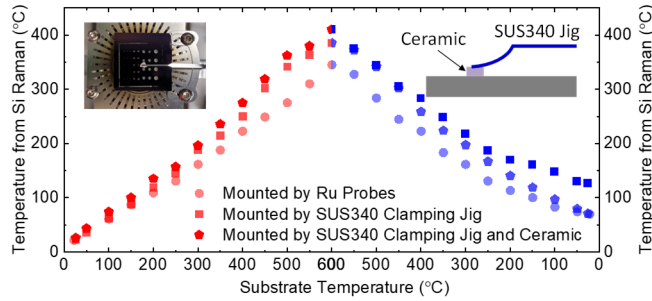

Fig. 9. Temperature calibration based on Si Raman thermometry measured from the same chip mounted on the heater and clamped by Ru probes, SUS340 clamping jig, and a ceramic piece, respectively. The inset shows the diagram of the chip anchored by the SUS340 clamping jig and the ceramic piece.

III. Conclusion

In summary, we have demonstrated AlScN/SiC thin-film micromachined diaphragm multimode resonators operating in high-temperature environment up to 600°C. We obtain an average TCf of less than 1 ppm/°C from the first resonant mode of the resonator with d =250 μm between 25°C to

200°C, and an average TCf of -17 ppm/°C between 200°C and 600°C. The repeatable resonance results taken from the heating and cooling processes indicates that the AlScN/SiC diaphragm resonators can be operated at high temperature up to 600°C reliably. Raman results show that the turning point of the peak position of the LO mode of both 3C-SiC and AlScN occurs at almost the same temperature range where the turning of TCf is observed. We have carefully calibrated the device temperature via measuring Si Raman peak, with the lattice temperature of 410ºC while the heater temperature is 600ºC. The heating efficiency can be further improved by using a clamping jig with lower thermal conductivity.

Acknowledgment

References

[1] P. X.-L. Feng, D. J. Young, and C. A. Zorman, MEMS/NEMS Devices and Applications (Chapter 13), in B. Bhushan (Eds.) *Springer Handbook of Nanotechnology*, 2017, pp. 395-429.

[2] O. Solgaard, A. A. Godil, R. T. Howe, L. P. Lee, Y. Peter, and H. Zappe, "Optical MEMS: From micromirrors to complex systems," *J. Microelectromech. Syst.*, vol. 23, no. 3, pp. 517-538, 2014.

[3] N. Marsi, B. Y. Majlis, A. A. Hamzah, and F. Mohd-Yasin, "High reliability of MEMS packaged capacitive pressure sensor employing 3C-SiC for high temperature," *Energy Procedia*, vol. 68, pp. 471-479, 2015.

[4] T. G. Brown, "Harsh military environments and microelectromechanical (MEMS) devices," in *Proc. IEEE SENSORS*, Toronto, ON, Canada, Oct. 22-24, 2003, pp. 753-760.

[5] A. Chaalane, R. Chemam, M. Houabes, R. Yahiaoui, A. Metatla, B. Ouari, N. Metatla, D. Mahi, A. Dkhissi, and D. Esteve, "A MEMS-based solid propellant microthruster array for space and military applications.," *J. Phys: Conf. Ser.*, vol. 660, no. 1, art. no. 012137, 2015.

[6] W. Sui, X.-Q. Zheng, J.-T. Lin, B. W. Alphenaar, and P. X.-L. Feng, "Thermal response and TCf of GaN/AlN heterostructure multimode micro string resonators from −10°C up to 325°C," *J. Microelectromech. Syst.*, vol. 30, no. 4, pp. 521-529, 2021.

[7] H. Chen, H. Jia, W. Liao, V. Pashaei, C. N. Arutt, M. W. McCurdy, C. A. Zorman, R. A. Reed, R. D. Schrimpf, M. L. Alles, and P. X.-L. Feng, "Probing heavy ion radiation effects in silicon carbide (SiC) via 3D integrated multimode vibrating diaphragms," *Appl. Phys. Lett.*, vol. 114, no. 10, art. no. 101901, 2019.

[8] A. Qamar, H. P. Phan, T. Dinh, N. T. Nguyen, and M. Rais-Zadeh, "ScAlN/3C-SiC/Si platform for monolithic integration of highly sensitive piezoelectric and piezoresistive devices," *Appl. Phys. Lett.*, vol. 116, no. 13, art. no. 132902, 2020.

[9] G. Esteves, S. D. Habermehl, P. J. Clews, C. Fritch, and B. A. Griffin, "AlN/SiC MEMS for high-temperature applications," *J. Microelectromech. Syst.*, vol. 28, no. 5, pp. 859-864, 2019.

[10] W. Sui, X.-Q. Zheng, J.-T. Lin, B. W. Alphenaar, and P. X.-L. Feng, "Temperature dependence of multimode gallium nitride/aluminum

nitride (GaN/AlN) heterostructure string resonator," in *Proc. IEEE 34th Int. Conf. Micro Electro Mech. Syst. (MEMS)*, Online/Virtual, Jan. 25-29, 2021, pp. 478-481.

[11] W. Sui, H. Wang, J. Lee, A. Qamar, M. Rais-Zadeh, and P. X.-L. Feng, "AlScN-on-SiC thin film micromachined resonant transducers operating in high-temperature environment up to 600°C," *Adv. Funct. Mater.*, art. no. 2202204, 2022.

[12] R. Deng, K. Jiang, and D. Gall, "Optical phonon modes in $Al_{1-x}Sc_xN$," *J. Appl. Phys.*, vol. 115, no. 1, art. no. 013506, 2014.

[13] A. L. Mock, A. G. Jacobs, E. N. Jin, M. T. Hardy, and M. J. Tadjer, "Long-wavelength dielectric properties and infrared active optical phonon modes of molecular beam epitaxy $ScxAl_{1-x}N$ determined by infrared spectroscopic ellipsometry," *Appl. Phys. Lett.*, vol. 117, no. 23, art. no. 232107, 2020.

[14] G. S. Chung and K. S. Kim, "Raman scattering of polycrystalline 3C–SiC film deposited on AlN buffer layer by using CVD with HMDS," *Microelectronics J.*, vol. 39, no. 12, pp. 1405-1407, 2008.

[15] Y. Tanaka, Y. Hasebe, T. Inushima, A. Sandhu, and S. Ohoya, "Comparison of AlN thin films grown on sapphire and cubic-SiC substrates by LP-MOCVD," *J. Cryst. Growth*, vol. 209, no. 2-3, pp. 410-414, 2000.